We are IntechOpen,
the world's leading publisher of
Open Access books
Built by scientists, for scientists

6,900
Open access books available

185,000
International authors and editors

200M
Downloads

Our authors are among the

154
Countries delivered to

TOP 1%
most cited scientists

12.2%
Contributors from top 500 universities

CLARIVATE ANALYTICS
BOOK CITATION INDEX
INDEXED

WEB OF SCIENCE™

Selection of our books indexed in the Book Citation Index
in Web of Science™ Core Collection (BKCI)

Interested in publishing with us?
Contact book.department@intechopen.com

Electrically-Driven Active Plasmonic Devices

Young Chul Jun

Additional information is available at the end of the chapter

1. Introduction

Enhanced light-matter interactions in light-confining structures (such as optical cavities) have been extensively investigated for both fundamental studies and practical applications. Plasmonic nanostructures, which can confine and manipulate light down to the nanometer scale, are becoming increasingly important (Atwater 2007, Brongersma 2009). Plasmonic resonators and antennas can convert free-space light into intense, localized fields or enable coupling into deep-subwavelength-guided modes. Wherever subwavelength control over light is required, plasmonic structures are likely to play a vital role. Strong field enhancement in those structures can also alter light-matter interactions at a very fundamental level. Many areas of optical physics and devices can benefit from such extreme light concentration and manipulation (Schuller 2010). Moreover, these metal nanostructures can be simultaneously used as electrical contacts for current injection or application of electric fields (MacDonald 2010, Cai 2012). Thus, plasmonic structures are naturally suited for electrically driven devices. These active plasmonic devices can enable a broad range of new opto-electronic applications.

In this chapter, we review device concepts for electrically-driven active plasmonic devices, including the author's own work. We divide the following sections based on the physical mechanism leading to electrical control. In each section, the device operation and physics are explained. Finally, the conclusions and future prospects are presented.

2. Electric field induced liquid crystal reorientation

One possible way to obtain electrical control of plasmonic devices is to manipulate the refractive index of the dielectric medium adjacent to the metal surface. Liquid crystals (LCs) are an excellent example of such a tunable medium. The large broadband optical anisotropy of LCs makes them ideal for electrically tunable plasmonic structures (Kossyrev 2005, Chu 2006). For example, a E7 LC layer was employed in contact with metallic hole arrays, and

electrical tuning of surface plasmon dispersion and optical transmission properties has been recently demonstrated (Dickson 2008). Plastic spacers (~ 60 um thick) were used to create the LC cell between the perforated gold film and the indium tin oxide (ITO) glass used as a top electrode. The static electric field controlled the LC's orientation in the cell. When the electric field was applied, the LC preferentially aligned with the field which was perpendicular to the interface. The maximum refractive index variation corresponding to a 90° reorientation of the LC was $n_e - n_o = 0.21$. (Ordinary and extraordinary refractive indexes, perpendicular and along the LC orientation, are $n_o = 1.525$ and $n_e = 1.734$.) This, in turn, induced a change in the SPP effective index at the Au/LC interface (given by Eq. 1) (Raether 1988) and optical response of the plasmonic crystals.

$$n_{SPP} = \sqrt{\varepsilon_{Au}\varepsilon_{LC} / (\varepsilon_{Au} + \varepsilon_{LC})} \qquad (1)$$

Changes in both transmission amplitude and resonance frequency were observed. The changes in the transmission near the band-edges of the plasmonic crystals were most prominent, as expected.

3. Electrically induced thermal heating or phase transition

Another approach for electrical control is based on electrically induced thermal heating or phase transition. Figure 1a shows a 'thermo-plasmonic' device based on electrically-driven thermal heating and refractive index changes in a thermo-optic polymer (Nikolajsen 2004). Long-range (LR) surface plasmon polariton (SPP) waveguides for a wavelength of 1.55 μm were utilized to implement Mach-Zender interferometric modulators (MZIMs) and directional-coupler switches (DCSs) (Fig. 1a). First, 15 nm thin and 8 μm wide gold stripes were sandwiched between 15 μm thick layers of a thermo-optic polymer (BCB, benzocyclobutene) and heated by electrical signal currents. The LRSPP mode was excited by end-fire coupling with a single mode fiber. Gold stripes worked simultaneously as plasmonic waveguides and electrical heating elements. This configuration maximizes the influence of applied electrical signals. Low driving powers (< 10 mW for modulators and < 100 mW for switches), high extinction ratios (> 30 dB), and moderate response times (~ 1 ms) were demonstrated.

The dissipated power in the device for the temperature increase ΔT can be estimated as $P \sim 2\kappa \, \Delta T L w/d$, where $\kappa \sim 0.2$ W/mK is the polymer thermal conductivity, $w = 8$ μm is the stripe width, and $d = 15$ μm is the cladding thickness. The temperature increase needed for complete extinction at the modulator output is given as $\Delta T = (\partial n/\partial T)^{-1}(\lambda/2L)$, where $\partial n/\partial T \sim -2.5 \times 10^{-5}$ °C^{-1} is the polymer thermo-optic coefficient. Thus, the estimate for the modulator driving power is obtained as $P \sim 2\kappa \, \Delta T L w/d = (\partial n/\partial T)^{-1}(\kappa w \, \lambda/d) \approx 7$ mW, which is close to the measured value.

More recently, a semiconductor based electrical tuning of extraordinary optical transmission (EOT) through a metal hole array was reported (Shaner 2007). The gold aperture array, designed to operate in the mid-infrared spectral range (~ 1200 cm^{-1}), was fabricated on a doped GaAs epilayer (Fig. 1b). When the current flowed under the metal grating layer, the

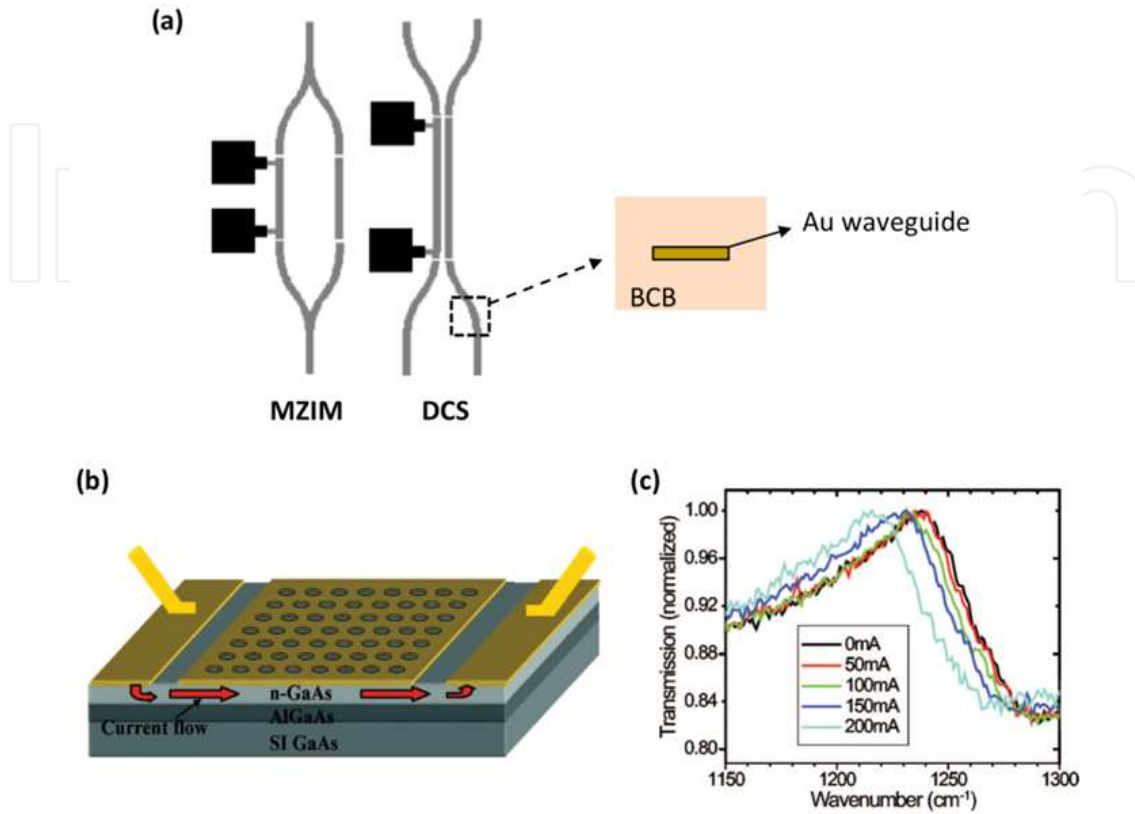epilayer was resistively heated, and frequency tuning of the EOT spectrum (over 25 cm^{-1}) was achieved (Fig. 1c).

Figure 1. Active plasmonic devices based on electrically induced thermal heating (Nikolajsen 2004, Shaner 2007). (a) Schematic of LRSPP-based plasmonic modulator and switch using an electrically-driven refractive index change in a thermo-optic polymer (BCB). (b) Schematic of a tunable EOT device. The current path through n-doped GaAs epilayer is shown. (c) Transmission spectra through the EOT device. A redshift is observed as the current level increases.

Light transmission through such a structure relies on surface plasmon (SP) excitations at the air/metal and metal/semiconductor interfaces. The SP resonance condition for the metal/semiconductor interface is approximately given by

$$\sqrt{i^2 + j^2}\,\lambda = a_0 \,\mathrm{Re}\!\left(\sqrt{\frac{\varepsilon_s \varepsilon_m}{\varepsilon_s + \varepsilon_m}} \right) \tag{2}$$

Here, λ is the free space wavelength, a_0 is the lattice constant, i and j are integers (related to reciprocal lattice vectors), and ε_s and ε_m are the permittivities of the semiconductor and metal. Thermal heating of the semiconductor layer affects both a_0 and ε_s, and thus induces the spectral tuning of the transmission peak. Thermal expansion of the heated sample can change a_0, which would lead to a red-shift in the SP resonance (Eq. 2). However, this is a relatively small effect. The semiconductor dielectric constant ε_s can be affected by temperature in several ways. The temperature dependence of the dielectric function can be modelled using the Drude approximation:

$$\varepsilon(\omega, T, N) = \varepsilon_\infty(T) \left(1 - \frac{\omega_p(T,N)^2}{\omega^2 + i\omega\Gamma(T,N)} \right) \quad \text{where} \quad \omega_p(T,N)^2 = \frac{N(T)q^2}{\varepsilon_0\varepsilon_\infty(T)m^*(T,N)} \tag{3}$$

Here, ε_∞ is the background high frequency dielectric constant, ω_P is the plasma frequency, N is the electron density, m^* is the electron effective mass, and Γ is the damping term (= $1/\tau$, τ is the electron scattering time). The sample temperature T can be determined by monitoring the GaAs bandgap change (e.g. measuring the band edge PL as a function of current). High sample temperature can increase thermal generation of free carriers and affect the dielectric constant. This also affects the electron scattering time and effective mass.

Electrically induced domain switching or phase transition can modify the substrate refractive index too. Recently, domain switching in the ferroelectric barium-titanate ($BaTiO_2$) thin film was employed for active plasmonic devices (Dicken 2008). $BaTiO_2$ is a perovskite ferroelectric material that exhibits a large electrooptic coefficient (on the order of $r \sim 100$ pm/V) and large birefringence $\Delta n = 0.05$ (ordinary and extraordinary indexes are $n_o = 2.412$ and $n_e = 2.36$, respectively). The application of a bias across an $Ag/BaTiO_2$ SPP waveguide induced domain switching in the $BaTiO_2$ film. This modified the refractive index in the ferroelectric layer and modulated the optical output of a plasmonic interferometric device (working at $\lambda_0 = 688$ nm) by up to 15%.

Related works on tunable terahertz metamaterials (MMs) use phase transition in vanadium dioxide (VO_2) (Driscoll 2009). VO_2 is a correlated electron material that exhibits an insulator-to-metal (IMT) phase transition which can be controlled thermally, electrically, or optically. Local heating by electrical current through the VO_2 film induced the IMT and a change in the refractive index of the film. With increased temperature, the refractive index of VO_2 increased and the MM resonance frequency red-shifted. This electrically controlled frequency tuning is highly hysteretic and persistent; thus, this MM/VO_2 structure can also be used as a memory device. Similar electro-optic switching of plasmonic metamaterials was demonstrated in the near-infrared region, using the transition between crystalline and amorphous phases in a chalcogenide glass layer (Samson 2010).

4. Electrical carrier injection or depletion in semiconductor structures

We have so far considered electrical control based on liquid crystal reorientation, thermal heating, phase transition, etc. These are attractive enough for some applications, but they are rather slow processes. Therefore, for other applications, faster electrical control based on conventional semiconductor device technology may be preferred. Electrical tuning via carrier injection or depletion in semiconductor structures has been widely studied for dielectric photonics structures, e.g. for high speed, compact silicon photonic modulators (Soref 1987, Reed 2010). Carrier injection or depletion modifies the refractive index of a medium and can induce a change in the behavior of dielectric resonators.

A similar concept has been applied to active tuning of plasmonic MMs at terahertz frequencies (Chen 2006, Chan 2009). The free carrier absorption in a doped-GaAs substrate

was dynamically controlled with an electric bias, by changing the carrier concentration in the substrate; this causes a strong amplitude modulation in the MM transmission. However, at higher frequencies (such as mid-infrared or mid-IR), the free carrier absorption is much smaller, so the transmission amplitude cannot be modulated in this way.

Nevertheless, using highly-doped semiconductor layers, we can still induce spectral tuning of mid-IR resonances by changing the refractive index of the substrate. Recently, electrically tunable mid-IR MMs based on depletion-type semiconductor devices was demonstrated (Jun 2012-1). Gold split ring resonator (SRR) arrays work simultaneously as an optical MM layer and electrical metal gate. With a reverse bias applied to the metal gate, the refractive index of the substrate directly underneath the plasmonic resonators varies through changes in the depletion width in a highly doped semiconductor. This results in frequency tuning of MM resonances. The mid-IR spectral range is technologically important for a number of applications, including chemical sensing and thermal imaging.

The images and schematics of the device are shown in Figs. 2a and 2b. The gold SRRs are connected to a metal gate via electrical bus lines and the whole MM layer works as an electrical gate. The MM layer is placed on top of an n-doped GaAs epilayer to form a metal-semiconductor junction. We need a highly doped n+ layer in order to induce a large dielectric constant change. An insulating barrier (e.g. undoped $Al_{0.3}Ga_{0.7}As$ layer) is also included to reduce leakage current. A modified SRR geometry was chosen because of its strong field enhancement in the two gaps and its compatibility with electrical connectivity, but other MM geometries can be used too.
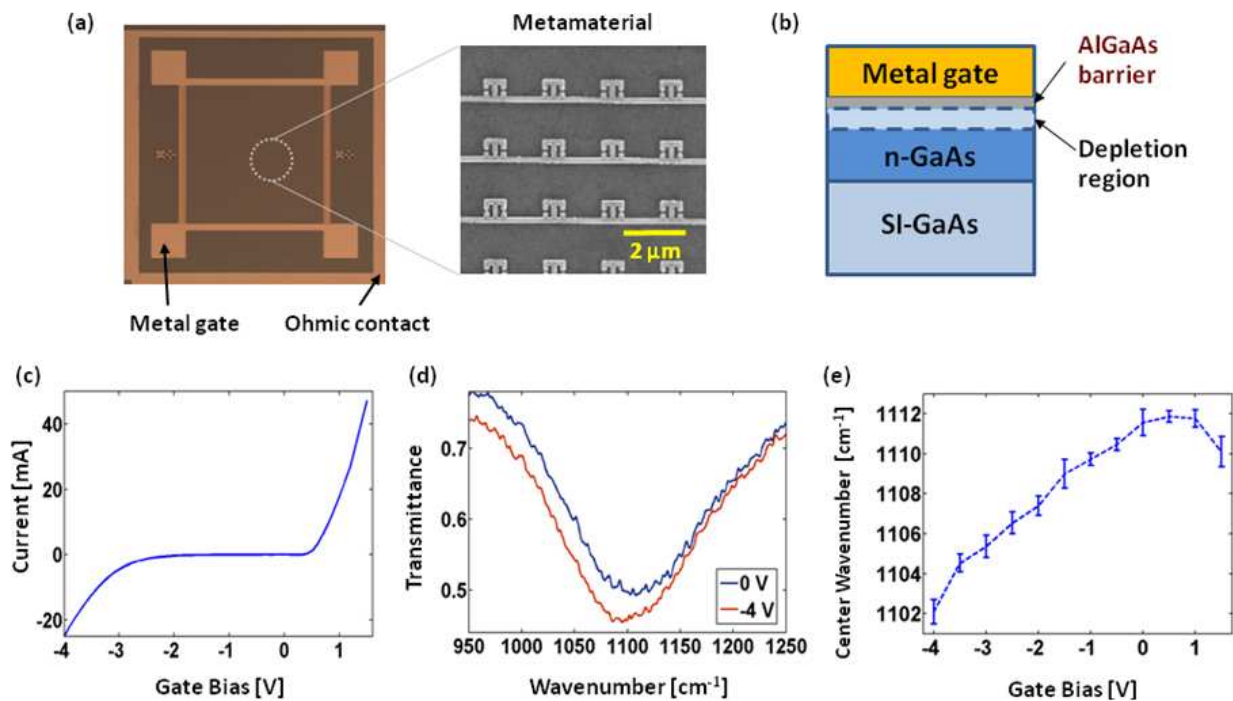

Figure 2. Fig. 2. Device structure and Measurement data (Jun 2012-1). (a) Image showing the device structure. The metamaterial layer (1 mm x 1 mm in size) is connected to the metal gate. These are surrounded by the outer Ohmic contact pad which contacts the n-doped layer. (b) Schematic of the substrate. It is composed of the barrier (30 nm $Al_{0.3}Ga_{0.7}As$) and doped semiconductor (n-GaAs, N_D = 5 x

10^{18} cm^{-3}) regions. The depletion region width in n-GaAs is varied by applying an external voltage. (c) IV curve exhibits a diode contact behavior. (d) Fourier transform infrared spectroscopy (FTIR) transmission measurement at room temperature for gate biases V$_G$ = 0 V and -4 V. (e) The center frequency of the metamaterial resonance as a function of gate bias.

The dielectric constant ε of a semiconductor substrate can be modeled using the Drude approximation (Eq. 3). In the high doping regime (> 10^{18} cm^{-3}), the dielectric constant decreases rapidly with doping density (Fig. 3a). So, starting from an n+ GaAs doped layer, we can remove carriers with a reverse bias by increasing the depletion region to obtain a large dielectric constant change (e.g. Δε ~ 5.5 for ΔN$_D$ = 5 x 10^{18} cm^{-3}, λ$_0$ = 10 μm).
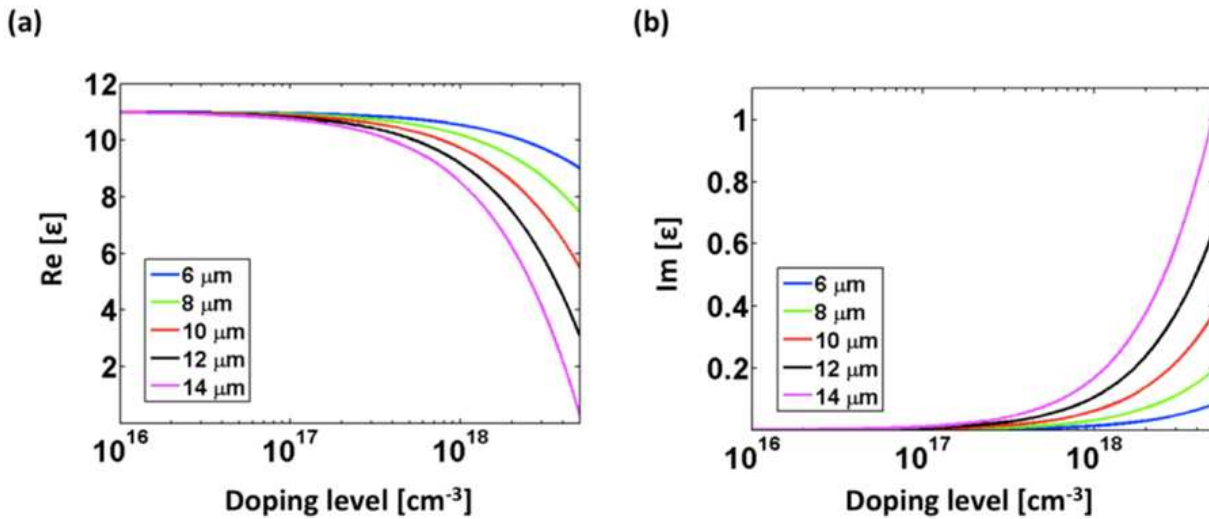

Figure 3. Drude model calculations of dielectric constants in n-doped GaAs for several mid-IR wavelengths (Jun 2012-1). (a) is the real part and (b) is the imaginary part of the dielectric constant.

The depletion width changes in an n-doped GaAs layer can be estimated using a textbook formula for a MIS (metal-insulator-semiconductor) capacitor:

$$W = \left[\frac{2\varepsilon_{GaAs}\varepsilon_0}{qN_D}(-\phi_s) \right]^{1/2} \tag{4}$$

where the surface potential ϕ_s is related to the gate voltage V$_G$ as follows:

$$V_G = \phi_s - \frac{\varepsilon_{GaAs}}{\varepsilon_{AlGaAs}} W_{barrier} \left[\frac{2qN_D}{\varepsilon_{GaAs}\varepsilon_0}|\phi_s| \right]^{1/2} + \phi_{MS} \tag{5}$$

Here, ϕ_{MS} is the flat-band voltage. Note that the dielectric constants here are static values, which are different from the high frequency ones in Eq. 1. The surface potential ϕ_s is introduced to consider a voltage drop across a barrier layer and obtain the actual voltage bias applied in the doped semiconductor region. The depletion width gradually increases with a reverse bias, and the width change depends on the doping density, barrier material/thickness, etc.

We can model the MM resonance shifts using electromagnetic simulations. Here, finite difference time domain (FDTD) simulations are used to simulate the transmission spectra. We utilize dielectric constants and depletion widths obtained by previous equations. The wavelength-dependent dielectric constants from the Drude model are used for a doped semiconductor layer. We employ a different depletion width for each bias and repeat the numerical simulation. A broadband light pulse is incident from the top (normal to the MM plane) and polarized orthogonal to the SRR gap to excite the lowest MM resonance. The transmission is measured on the substrate side.

Figure 4 shows the calculated transmission spectrum. The transmission dip shows a spectral shift upon the application of a bias (Fig. 4a) and gradually red-shifts with increasing reverse bias (Fig. 4b) in agreement with our measurements. This red-shift can be easily understood from a LC resonator model. From $\omega_0 = 1/\sqrt{LC}$, we have $\omega_0 \propto 1/\sqrt{\varepsilon} = 1/n$, where n is the refractive index of a substrate. When the depletion width increases, the substrate refractive index increases (Fig. 3a) and the resonance red-shifts.
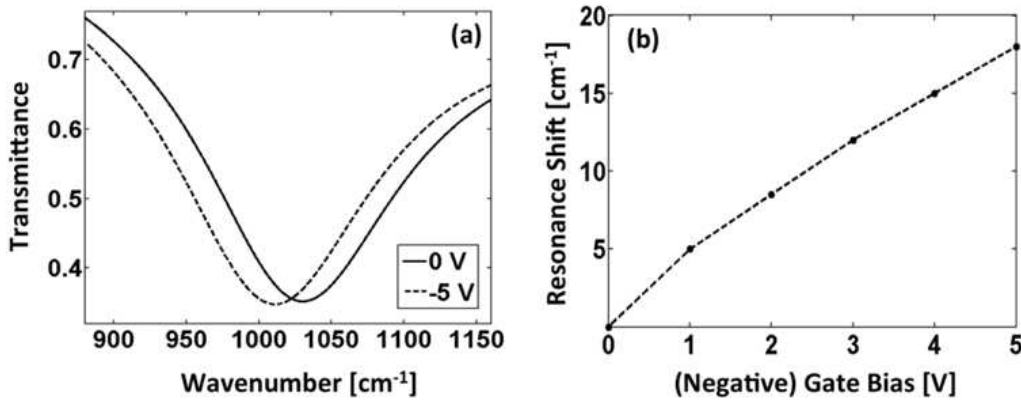

Figure 4. FDTD simulations of MM transmission spectra (Jun 2012-1). (a) Transmission spectra for the gate bias V$_G$ = 0 V and -5 V. (b) Resonance red-shift as a function of reverse bias to the gate.

Electrical tunability can be further increased using asymmetric metamaterial designs (Jun 2012-2), which can be more sensitive to a substrate permittivity change. Recently, a classical analog of electromagnetically induced transparency (EIT) was demonstrated in several plasmonic and metamaterial structures. One such structure consists of two metal arcs with different lengths in order to have resonances at slightly different frequencies (Fig. 5, inset). The two metal arms are out-of-phase within a narrow frequency range, and the transmission spectrum has a transparency window due to the destructive interference from two resonator arms. Because this transparency window is caused by interference from two coupled resonators, it can be more sensitive to a substrate refractive index change. Figure 5a shows the simulated transmission spectrum for several different gate biases. We find that the interference part has larger tuning than other frequencies, as expected.

Depletion-type devices are also good for local index control. We can electrically address each resonator arm separately (Figs. 5a-5c). Depending on the bias scheme, we obtain quite different tuning behaviors. Here, we show a two-coupled resonator case. However, more sophisticated structures can be designed to enable a tailored spectrum change with a voltage

bias. Electrically tunable metamaterials can be used for novel active infrared devices, such as optical filters, switches, modulators, and phase shifters.
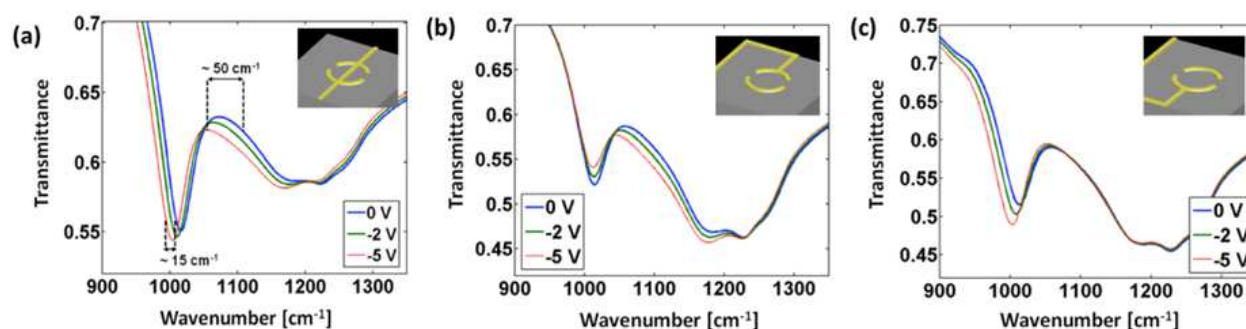

Figure 5. Asymetric metamaterial design based on coupled resonators (Jun 2012-2). Simulated transmission spectrum for several different gate biases, where (a) both resonator arms are connected to an electrical bus line – the straight gold line in the inset – and electrically biased, (b) only the smaller arc is connected to the electrical bus line, (c) only the larger arc is connected. The inset shows the unit cell of the FDTD simulation.

Other semiconductor structures or materials can be also adopted. For example, a metamaterial layer can be patterned on quantum well or quantum dot substrates to induce optical coupling between them (Gabbay 2011). The frequency and strength of this optical coupling can be tailored by designing proper metamaterial/substrate structures. Furthermore, this coupling can be electrically tuned by the stark shift of the quantum well or quantum dot transitions (Gabbay 2012), for instance. Graphene can be also employed for tunable plasmonic metamaterials. Due to its high polarizability, a single atomic layer of graphene can induce a noticeable change in the optical response of metamaterials (Papasimakis 2010). Electrostatic gating can be used to actively tune the optical response of graphene (Wang 2008), thus inducing a change in metamaterial responses. ITO can be also used for electrically carrier injection to induce a change in plasmonic mode indexes at visible and near-infrared wavelengths (Feigenbaum 2010).

A conventional metal-oxide-semiconductor (MOS) capacitor can be utilized as a plasmonic waveguide. Recently, a MOS field-effect plasmonic modulator was reported, termed a 'plasMostor' (Dionne 2009). That employs a metal-MOS-metal (Ag-SiO2-Si-Ag) waveguide structure, operating at 1.55 μm. It supports both photonic and plasmonic modes and has a transmission coefficient determined by interference between them; e.g., application of a gate bias (> 0.7 V) drives the MOS into accumulation and changes the Si index, which cut off the photonic mode and induces the transmission change. This plasmonic modulator can achieve modulation ratios approaching 10 dB in device volumes of half a cubic wavelength with femtojoule switching energies and the potential for gigahertz modulation frequencies.

5. Electrically pumped plasmon-emitting diode

The excitation of SPs with free-space light requires a special momentum matching technique (such as prism coupling, gratings, or scatterers). However, if the metal surface is very close to a light emitter (e.g. fluorescent molecules or quantum dots), the SPs can be excited

directly via near-field coupling. Metal layers that support and guide the SP mode can also serve as contact electrodes. This brings an interesting opportunity for electrically pumped SP sources. The development of such electrical SP sources is important for miniaturized photonic circuitry and integrated sensing platforms.
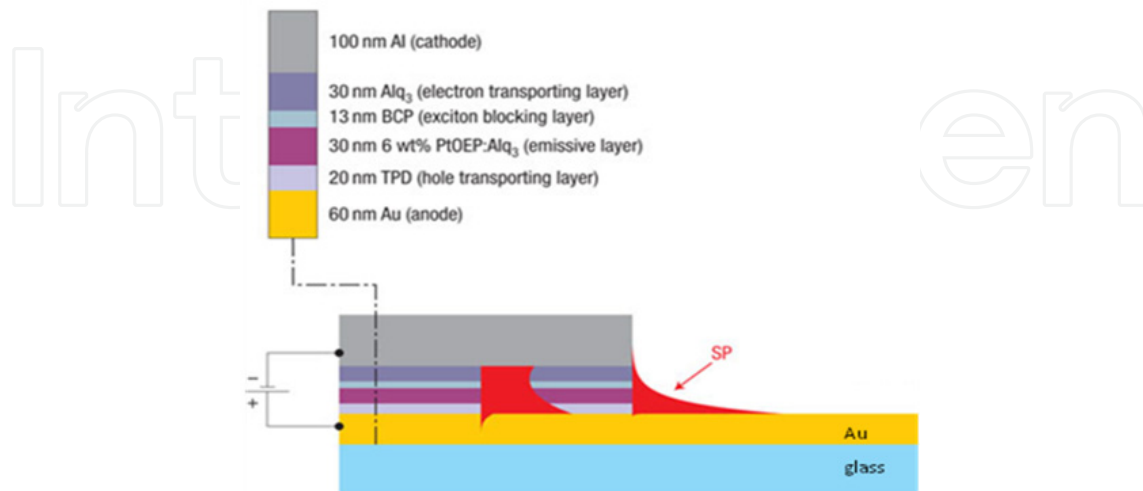

Figure 6. Schematic of an organic plasmon-emitting diode (Koller 2008). SPs are excited electrically through exciton recombination inside the MDM waveguide and later outcoupled to single surface SP wave as shown above.

Figure 6 shows an electrically pumped SP source using organic light-emitting diode (OLED) structures (Koller 2008). The organic active layers are placed in between two gold layers (i.e., a metal-dielectric-metal structure, or MDM). Metal layers work simultaneously as the SP waveguide and metal electrode. Electrically injected electrons and holes recombine in the active organic layer and generate the SP wave. The excited SP mode in the MDM waveguide can extend further into a single metal surface as shown in Fig. 6. The strong electromagnetic field intensity of the SP mode can enable a compact sensing platform without external illumination optics.
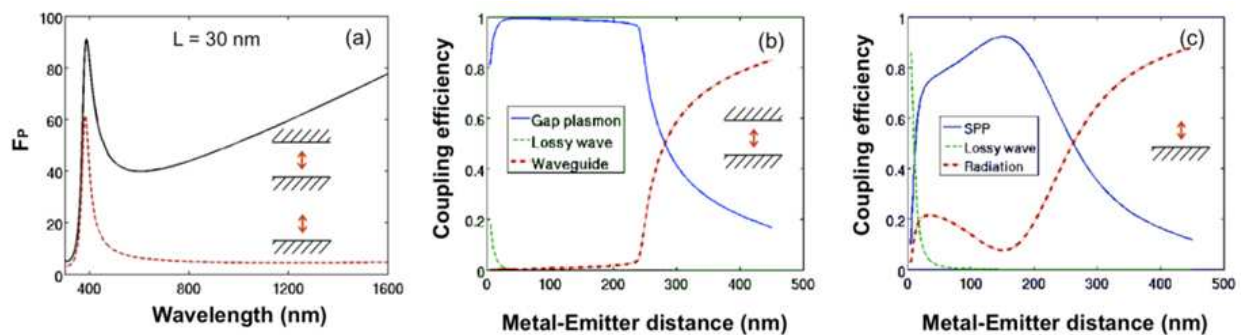

Figure 7. Light emission of a dipolar emitter inside an Ag/SiO$_2$/Ag MDM slab waveguide or near an Ag/SiO$_2$ interface (Jun 2008). We assume that the emitter has unit quantum efficiency. (a) Spontaneous emission enhancement as a function of free-space wavelength. In the MDM case, the emitter is in the center of the gap. The gap size L = 30 nm. (b) Fraction of dissipated energy into different decay pathways as a function of the metal-emitter distance. The emission wavelength λ_0 = 800 nm. (c) same as (b) but for the single metal/dielectric interface case.

A similar electrical SP source based on silicon CMOS processes has been reported (Walters 2010): gold cladding layers surround a semi-insulating layer of alumina that contains silicon quantum dots and form a MDM plasmonic waveguide. When a sufficient voltage is applied across the insulator layer, tunnelling electrons can excite the embedded quantum dots through impact ionization processes, producing the SP wave. The device fabrication and materials are compatible with well-established silicon microelectronics processes.

Because of their small optical mode volume, MDM structures can achieve large spontaneous emission enhancement and high coupling ratio into well-defined SPP waveguide modes (Jun 2008). Figure 7 explains this for a single dipolar emitter which is oriented normal to the interfaces. The spontaneous emission enhancement factor, F_P, is obtained by calculating the work done on the dipole by its own reflected field from the metal surfaces. Figure 7a shows F_P as a function of the free-space wavelength. In addition to a resonant enhancement peak around the SP resonance wavelength of silver, there is a strong non-resonant enhancement due to the tight confinement of modes between the two metallic films. In the non-resonant region, propagation lengths of SP modes become longer, which is desirable for many applications. For comparison, the case of a single metal surface is also plotted (dashed line), which clearly lacks such non-resonant enhancement. The light emission in MDM waveguides is also preferentially directed into plasmonic waveguide modes (Fig. 7b) over a large range of gap sizes. This behavior is in stark contrast to that observed for an emitter near a single metal surface, which exhibits relatively stronger coupling to lossy surface waves and free-space modes (Fig. 7c).
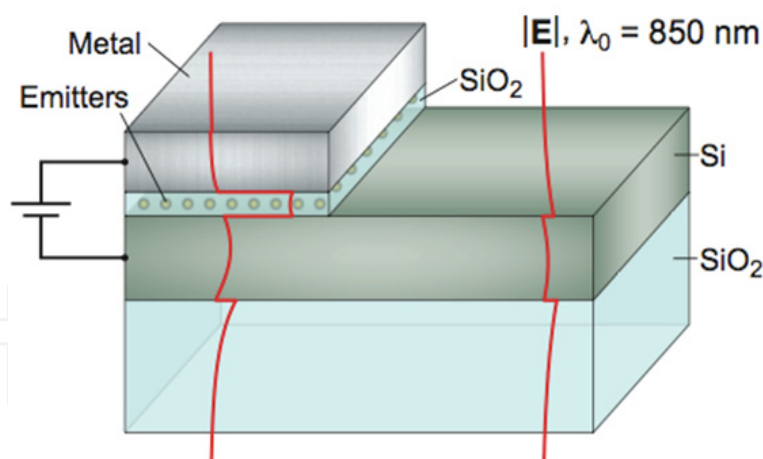

Figure 8. Schematic of a CMOS-compatible light-emitting device (Hryciw 2009). Typical electric field profiles for a TM mode are shown in red. Electrically pumped light emission in the MDS waveguide excites hybrid plasmonic modes and later can be outcoupled to SOI waveguide modes.

A high-index silicon slab supports guided dielectric modes. When this silicon slab is brought closer to a metal surface which supports SPP modes, a new hybrid plasmonic mode can form. A metal-dielectric-semiconductor (MDS) structure resembles MOS layers in conventional semiconductor devices and thus can be used as CMOS-compatible light sources. We can still achieve large field enhancement in the low-index dielectric region of

such hybrid structures. Spontaneous emission enhancement in MDS waveguides is still significantly larger than those from a single metal surface. MDS waveguides exhibit broadband emission enhancement and high waveguide coupling ratio, similar to MDM waveguides (Hryciw 2009, Hryciw 2010). Furthermore, this MDS structure is more suitable for electrical carrier injection. The plasmonic modes in MDS waveguides can be efficiently converted into silicon slab waveguide modes for a longer distance transport (Fig. 8).

In addition to these plasmon-emitting diodes, there have been demonstrations on nanocavity lasers based on electrically pumped metal-coated cavities, MDM waveguides, and optically pumped hybrid plasmonic cavities (Martin 2010). In a 'spaser' (surface plasmon amplification by stimulated emission of radiation), the lasing mode may even be non-radiating, i.e. a near-field laser. Such coherent nanoscale light sources can lead to new applications in sensing and lithography.

6. Electrical control of light emission in plasmonic nanogaps

It was recently demonstrated that nanopatterned metal films such as metal slit-grooves can collimate and direct quantum dot (QD) emission in a designed fashion, working effectively as optical antennas (Jun 2011). The patterned metal films next to a slit can be used as electrical contacts to apply a field across the slit. In this section, we consider active electrical control of QD emission in such plasmonic nanogaps. We show how the metals defining the plasmonic cavity can be utilized to electrically control the emission intensity and wavelength. The unmatched, combined directional and electrical control over the emission of a large number of quantum emitters opens up a broad range of new opto-electronic applications for plasmonic antennas, facilitating the realization of a new class of active optical antennas.
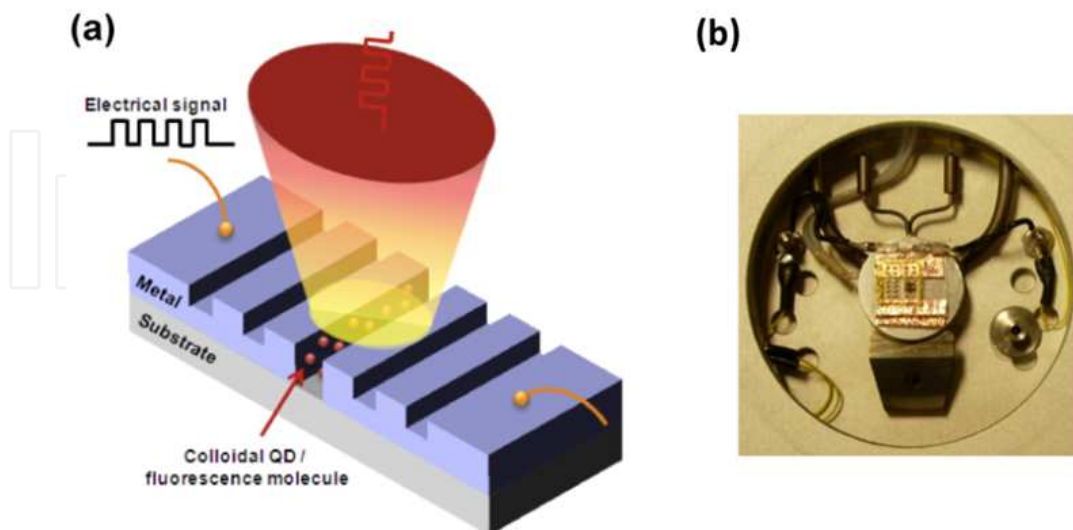

Figure 9. Electrical control of QD photoluminescence (Jun 2011). (a) Schematic of a plasmonic antenna device, in which colloidal CdSe/ZnS core/shell quantum dots are placed within the nanslit. An optical pump at 514 nm was directed from the below, and QD emission was collected from the top. (b) Top view of the mounted sample on the Linkam thermal stage.

First, two large metal contact pads were defined by standard optical lithography. Two metal pads were connected with a narrow metal stripe. A slit-groove structure was patterned later on this stripe with focused ion beam (FIB) milling (Fig. 9a). After FIB milling, the two metal pads were electrically disconnected. Then, a thin layer of colloidal CdSe/ZnS QDs mixed with PMMA (poly-methylmethacrylate) was spin-coated on top of the patterned metal structures. Electrical measurements were conducted at a low temperature using the Linkam thermal stage. A sample was mounted on the silver chuck of the Linkam thermal stage (Fig. 9b), which was cooled with liquid nitrogen flowing. Two metal contacts in the sample were wire-bonded for electric biasing. Because the chuck had a hole in the center, we could direct laser light (CW laser light at 532 nm) from the bottom and collect QD emission from the top. We applied external voltages across the metal gap to see the voltage-dependent QD emission spectrum.

Figure 10a shows the voltage-dependent QD emission spectrum measured from this slit-groove sample. As the applied DC voltage increases, the QD emission spectrum exhibited a red-shift and luminescence quenching. In most cases, the spectral changes were reversible by alternating external voltages, although sometimes QDs or the metal nanoslits were damaged under the strong field. The spectrum shift can be understood as the Stark effect of emission. The large electric field pulls apart electron-hole pairs inside QDs and induces the red-shift and broadening of the whole emission spectrum. Note that despite the intensity drop at the spectrum center, the QD emission intensity increased at longer wavelengths with applied voltages. However, the Stark effect alone does not explain the observed, large luminescence quenching. We believe this is possibly due to enhanced nonradiative recombination. A very large electric field in the gap can 'dissociate' electron-hole pairs, and those carriers can induce luminescence quenching by participating in nonradiative recombination processes such as Auger recombination.

Figure 10b shows the measured emission frequency shift as a function of applied voltage. The shift initially increases quadratically with voltage (as expected for the Stark shift) and then saturates at larger voltages (shaded region). According to quantum mechanical perturbation theory, the stark shift is given by

$$\Delta E = \mu F + \alpha F^2 + ... \qquad (6)$$

where F is the electric field magnitude, μ permanent dipole moment, and α polarizability. It is known that a CdSe QD has a Wurtzite crystal structure and a permanent dipole moment. Thus, depending on the orientation of a QD, we can observe either a red- or blue-shift with the applied external field. However, averaging over many QDs in the gap, the linear term cancels out, and we obtain only a quadratic stark shift (i.e. red-shift). Thus, for our QD ensemble measurement, we expect to see the quadratic red-shift with external field, in agreement with Fig. 10b.

We can deduce the polarizability of QDs from this Stark shift data: we first obtain the electric field magnitude inside a QD as a function of applied voltage. Assuming that a QD is a sphere dielectric, we can analytically calculate the electric field F_{in} inside the QD:

$$F_{in} = -\frac{d\varphi_{in}}{dr} = \frac{3}{\varepsilon_{QD}/\varepsilon_{matrix}+2}F_0 = \frac{3}{\varepsilon_{QD}/\varepsilon_{matrix}+2}\frac{V_a}{W} \tag{7}$$

where ε_{QD} and ε_{matrix} are the dielectric constants of QD and surrounding matrix medium, and F_0 is the incident field magnitude. The numbers 3 and 2 originate from the geometry (i.e. sphere).
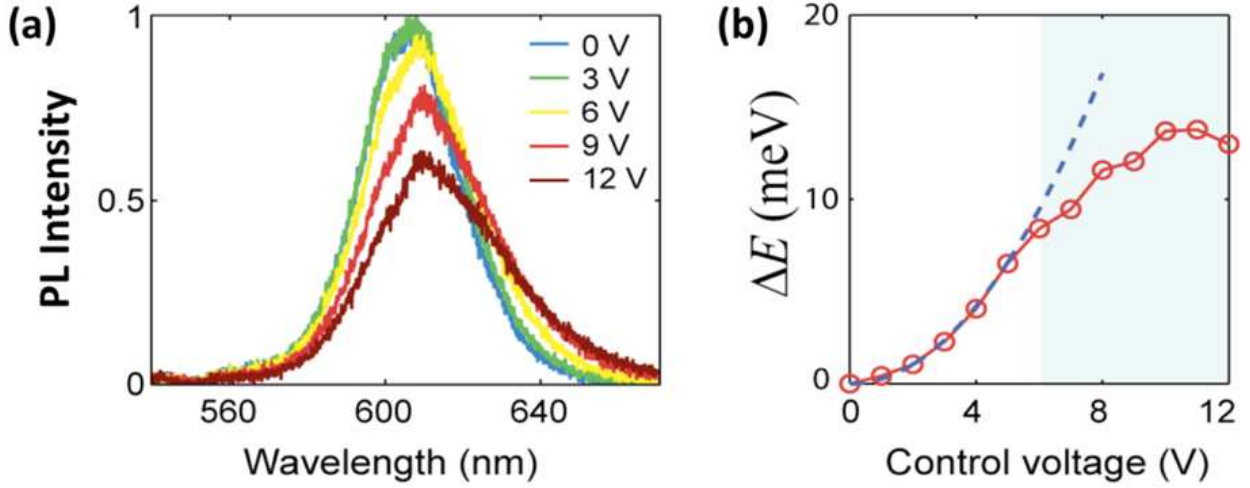

Figure 10. Bias-dependent QD emission (Jun 2011). (a) Emission spectra measured at different applied DC bias voltages across the nanogap. (b) The Stark shift of the emission as a function of applied voltage. The dashed line corresponds to a quadratic fitting curve, and the shaded region indicates a saturation effect for large voltages.

We have $F_0 = V_a/W$, considering that we have a voltage drop V_a across the gap W. In this experiment, we have $W = 60$ nm, $\varepsilon_{CdSe} = (2\varepsilon_\perp + \varepsilon_{||})/3 = 2/3 \times 9.23 + 1/3 \times 10.16 \approx 9.58$, $\varepsilon_{matrix} = \varepsilon_{PMMA} = 2.22$. By fitting data in Fig. 10b to the following equation (i.e. blue dotted curve in Fig. 10b), we obtain the QD polarizability.

$$\Delta E = \alpha F^2;\ \alpha = 4\times 10^{-5}\, meV \cdot cm^2/(kV)^2 \tag{8}$$

Furthermore, we can apply a time-varying voltage signal and modulate the QD emission dynamically (Fig. 9a). A square-wave voltage signal was applied across the gap with a function generator. A 100 kHz voltage signal modulated between 0V and 10V with a 50% duty cycle. The QD emission was detected with a single photon avalanche detector (SPAD). We used the sync signal of the function generator as a start signal and the SPAD output as a stop signal in the photon counting module (Picoharp 300, Picoquant) to obtain the accumulated histogram of the modulated QD emission intensity (Fig. 11). A clear step appears in the time-resolved histogram: this means that the QD emission intensity was modulated with the external voltage signal. We accumulated the SPAD output for a few minutes to obtain a clear modulation step. This improved the signal-to-noise ratio but did not change the actual modulation depth. A modulation depth of M ~ 24 % was achieved, where $M = (I_{max} - I_{min})/I_{max}$.

This step appears only when we see QD emission spectrum change with voltage. For example, if incident laser light illuminated QDs on the bare quartz region (i.e. outside the metal stripe), we did not observe such a modulation step. The histogram just appears flat, i.e. no voltage dependent change. We also note that the observed modulation depth also depends on the detection wavelength. When there is a large change in QD emission spectrum, we observed larger modulation depth. This result presents new opportunities for electrically modulated optical antenna devices. In the above experiment, the modulation speed was rather moderate (100 kHz), but we can increase the speed to well above 100 MHz.
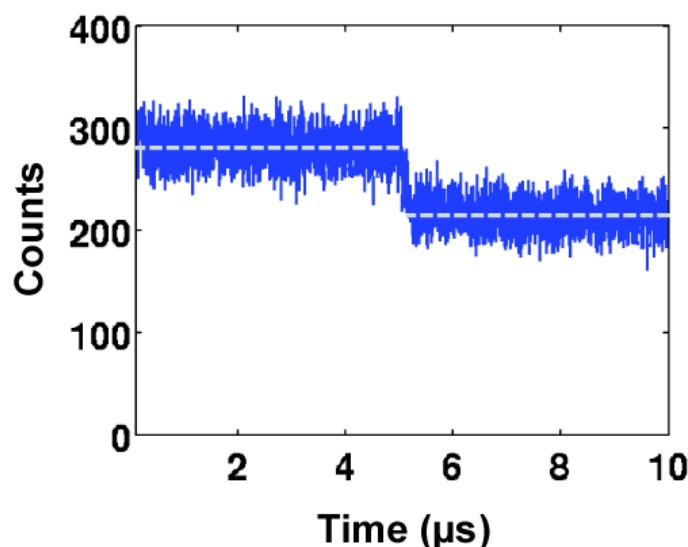

Figure 11. The time-resolved histogram of electrically modulated QD emission intensity (Jun 2011). The modulated square-wave signal (0-10 V, 100 kHz, 50% duty cycle) is applied. The step means that QD emission intensity is dynamically modulated with the external voltage signal.

Plasmonic modes in small metal nanogaps (< 100 nm) can further contribute to this electrical modulation. Spontaneous emission can be enhanced greatly in a small metal nanogap. The reduced lifetime can improve the responsivity of devices and increase the upper limit of the modulation speed. Furthermore, optimized side grooves can enable optical beaming. This electrically driven slit-groove structure acts as an active optical antenna, which can collimate and modulate QD emission in one device. The unmatched, combined directional and electrical control over the emission of a large number of quantum emitters can support a broad range of new opto-electronic applications.

More recently, electrically controlled nonlinear harmonic generation of light in plasmonic nanogaps was demonstrated (Cai 2011). The device structure is similar to the previous one (Fig. 9a). A commonly used polymer (PMMA, poly-methyl methacrylate) was inserted into the metal slit. The frequency doubled light originated from a third-order nonlinear susceptibility $\chi(2\omega; \omega, \omega, 0)$. The change in the second-harmonic signal as a function of applied DC voltage indicated a linear dependence of the frequency doubled output on the driving voltage, with the magnitude of the normalized change being over 7% per volt. Unlike the conventional second harmonic generation, which imposes a rigorous

requirement on the lattice asymmetry of the nonlinear medium, third-order nonlinear responses are present in all materials. The subwavelength device size also eases the strict phase-matching condition and makes them suitable for chipscale, high density integration.

7. Conclusions

Plasmonics is emerging as a new chip-scale device technology that can bridge the size mismatch between nanoscale electronics and microscale photonics. It can combine the size of electronics and the speed/bandwidth of photonics in one device. It exploits the unique optical properties of metallic nanostructures to confine and manipulate light at the nanoscale. Strong optical field enhancement in plasmonic nanostructures can also modify light-matter interactions to unprecedented levels. Furthermore, plasmonic structures can serve as electrodes and thus perform optical and electrical functions simultaneously. This brings about many new opportunities for opto-electronic devices.

This chapter reviewed novel active plasmonic device concepts explored in the literature, including the author's own work. Electrically driven plasmonic device structures were introduced, and their device operation and physics were explained. Various physical mechanisms can be utilized for electrical control of optical properties, such as liquid crystal reorientation, thermal heating, phase transition, carrier injection/depletion, Stark shift of emitters, etc. The next step would be to develop device structures that are more efficient, compact, and scalable for large area, dense integration.

Author details

Young Chul Jun
Center for Integrated Nanotechnologies (CINT), Sandia National Laboratories, NM, USA

Acknowledgement

8. References

Atwater, H.A. (2007), The promise of plasmonics, *Scientific American*, (April 2007), pp. 56-63

Brongersma, M.L. (2009), Schuller, J.A., White, J., Jun, Y.C., Bozhevolnyi, S.I., Sondergaard, T., Zia, R. Nanoplasmonics : components, devices, and circuits in *Plasmonic Nanoguides and Circuits*, (Pan Stanford Publishing, 2009), edited by Bozhevolnyi, S.I.

Cai, W. (2011), Vasudev, A.P., Brongersma, M.L. Electrically controlled nonlinear generation of light with plasmonics. *Science*, Vol.333, No.6050, (2011), pp. 1720-1723

Cai, W. (2012), Jun, Y.C., Brongersma, M.L. Electrical control of plasmonic nanodevices. SPIE Newsroom, (2012), doi: 10.1117/2.1201112.004060

Chan, W.L. (2009), Chen, H.-T., Taylor, A.J., Brener, I., Cich, M.J., Mittleman, D.M. A spatial light modulator for terahertz beams. *Appl. Phys. Lett.*, Vol.94, No.21, (2009), p. 213511

Chen, H.-T. (2006), Padilla, W.J., Zide, J.M.O., Gossard, A.C., Taylor, A.J., Averitt, R.D. Active terahertz metamaterial devices. *Nature*, Vol.444, (2006), pp. 597-600

Chu, K.C. (2006), Chao, C.Y., Chen, Y.F., Wu, Y.C., Chen, C.C. Electrically controlled surface plasmon resonance frequency of gold nanorods. Appl. Phys. Lett., Vol.89, No.10, (2006), p. 103107

Dicken, M.J. (2008), Sweatlock, L.A., Pacifici, D., Lezec, H.J., Bhattacharya, K., Atwater, H.A. Electrooptic modulation in thin film barium titanate plasmonic interferometers. *Nano Lett.*, Vol.8, No.11, (2008), pp. 4048-4052

Dickson, W. (2008), Wurtz, G.A., Evans, P.R., Pollard, R.J., Zayats, A.V. Electronically controlled surface plasmon dispersion and optical transmission through metallic hole arrays using liquid crystal. *Nano Lett.*, Vol.8, No.1, (2008), pp. 281-286

Dionne, J.A. (2009), Diest, K., Sweatlock, L.A., Atwater, H.A. PlasMOStor : a Metal-Oxide-Si field effect plasmonic modulator. *Nano Lett.*, Vol.9, No.2, (2009), pp. 897-902

Driscoll, T. (2009), Kim, H.-T., Chae, B.-G., Kim, B.-J., Lee, Y.-W., Jokerst, N.M., Palit, S., Smith, D.R., Ventra, M.D., Basov, D.N. Memory Metamaterials. *Science*, Vol.325, No.5947, (2009), pp. 1518-1521

Feigenbaum, E. (2010), Diest, K., Atwater, H.A. Unity-order index change in transparent conduction oxides at visible frequencies. *Nano Lett.*, Vol. 10, No. 6, (2010), pp. 2111-2116

Gabbay, A. (2011), Reno, J., Wendt, J.R., Gin, A., Wanke, M.C., Sinclair, M.B., Shaner, E., Brener, I. Interaction between metamaterial resonators and intersubband transitions in semiconductor quantum wells. *Appl. Phys. Lett.*, Vol. 98, No. 20, (2011), p. 203103

Gabbay, A. (2012), Brener, I. Theory and modeling of electrically tunable metamaterial devices using intersubband transitions in semiconductor quantum wells. Opt. Express, Vol.20, No.6, (2012), pp. 6584-6597

Hryciw, A. (2009), Jun, Y.C., Brongersma, M.L. Plasmon-enhanced emission from optically-doped MOS light sources. *Opt. Express*, Vol.17, No.1, (2009), pp. 185-192

Hryciw, A. (2010), Jun, Y.C., Brongersma, M.L. Electrifying plasmonics on silicon. *Nature Mater.*, Vol.9, (2010), pp. 3-4

Jun, Y.C. (2008), Kekatpure, R.D., White, J.S., Brongersma, M.L. Nonresonant enhancement of spotaneous emission in metal-dielectric-metal plasmon waveguide structures. *Phys. Rev. B*, Vol.78, No.15, (2008), p. 153111

Jun, Y.C. (2011), Huang, K.C.Y., Brongersma, M.L. Plasmonic beaming and active control over fluorescent emission. *Nature Comm.*, Vol.2, (2011), p. 283

Jun, Y.C. (2012-1), Gonzales, E., Reno, J.L., Shaner, E.A., Gabbay, A., Brener, I. Active tuning of mid-infrared metamaterials by electric control of carrier densities. *Opt. Express*, Vol.20, No.2, (2012), pp. 1903-1911

Jun, Y.C. (2012-2), Brener, I. Electrically tunable infrared metamaterials based on depletion-type semiconductor devices. *submitted* (2012)

Koller, D.M. (2008), Hohenau, A., Ditlbacher, H., Galler, N., Reil, F., Aussenegg, F.R., Leitner, A., List, E.J.W., Krenn, J.R. Organic plasmon-emitting diode. *Nature Photon.*, Vol.2, (2008), pp. 684-687

Kossyrev, P.A. (2005), Yin, A., Cloutier, S.G., Cardimona, D.A., Huang, D., Alsing, P.M., Xu, J.M. Electric field tuning of plasmonic response of nanodot array in liquid crystal matrix. Nano Lett., Vol.5, No.10, (2005), pp. 1978-1981

MacDonald, K.F. (2010), Zheludev, N.I. Active plasmonics : current status. *Laser Photonics Rev.*, Vol.4, No.4, (2010), pp. 562-567

Martin, T.H. (2010), Status and prospects for metallic and plasmonic nano-lasers. J. *Opt. Soc. Am. B*, Vol.27, No.11, pp. B36-B44.

Nikolajsen, T. (2004), Leosson, K., Bozhevolnyi, S.I. Surface plasmon polariton based modulators and switches operating at telecom wavelengths. *Appl. Phys. Lett.*, Vol.85, No.24, (2004), pp. 5833-5835

Papasimakis, N. (2010), Luo, Z., Shen, Z.X., Angelis, F.D., Fabrizio, E.D., Nikolaenko, A.E., Zheludev, N.I. Graphene in a photonic metamaterial, *Opt. Express*, Vo.18, No.8, (2010), pp. 8353-8359

Raether, H. (1988), *Surface Plasmons on Smooth and Rough Surfaces and on Gratings*, Springer-Verlag.

Reed, G.T. (2010), Mashanovich, G., Gardes, F.Y., Thomson, D.J. Silicon optical modulators. *Nature Photon.*, Vol.4, (2010), pp. 518-526

Samson, Z.L., MacDonald, K.F., Angelis, F.D, Gholipour, B., Knight, K., Huang, C.C., Fabrizio, E.D., Hewak, D.W., Zheludev, N.I. Metamaterial electro-optic switch of nanoscale thickness. *Appl. Phys. Lett.*, Vol.96, (2010), p. 143105

Schuller, J.A., Barnard, E.S., Cai, W., Jun, Y.C., White, J.S., Brongersma, M.L. Plasmonics for extreme light concentration and manipulation. *Nature Mater.*, Vol.9, (2010), pp. 193-204

Shaner, E.A. (2007), Cederberg, J.G., Wasserman, D. Electrically tunable extraordinary optical transmission gratings. *Appl. Phys. Lett.*, Vol.91, (2007), p. 181110

Soref, R.A. (1987), Bennett, B.R. Electrooptical effects in silicon. *IEEE J. Quantum Electron.*, Vol.QE-23, No.1, (1987), pp. 123-129

Walters, R.J. (2010), van Loon, R.V.A., Brunets, I., Schmitz, J., Polman, A. A silicon-based electrical source of surface plasmon polaritons. *Nature Mater.*, Vol.9, (2010), pp. 21-25

Wang, F. (2008), Zhang, Y., Tian, C.S., Girit, C., Zettl, A., Crommie, M.F., Shen, Y.R. Gate-variable optical transitions in graphene. Science, Vol.320, No.5873, (2008), pp. 206-209